Boundary-Layer Meteorol (2012) 145:229–248
DOI 10.1007/s10546-011-9631-3

ARTICLE

A Large-Eddy Simulation Study of Water Vapour and Carbon Dioxide Isotopes in the Atmospheric Boundary Layer

Xuhui Lee · Jianping Huang · Edward G. Patton

Received: 9 January 2011 / Accepted: 20 June 2011 / Published online: 10 July 2011

Abstract A large-eddy simulation model developed at the National Center for Atmospheric Research (NCAR) is extended to simulate the transport and diffusion of $C^{18}OO$, $H_2{}^{18}O$ and $^{13}CO_2$ in the atmospheric boundary layer (ABL). The simulation results show that the ^{18}O compositions of leaf water and the ABL CO_2 are moderately sensitive to wind speed. The variations in the ^{18}O composition of water vapour are an order of magnitude greater than those in the ^{13}C and ^{18}O compositions of CO_2 both at turbulent eddy scales and across the capping inversion. In a fully-developed convective ABL, these isotopic compositions are well mixed as with other conserved atmospheric quantities. The Keeling intercepts determined with the simulated high-frequency turbulence time series do not give a reliable estimate of the ^{18}O composition of the surface water vapour flux and may be a reasonable approximation to the ^{13}C and ^{18}O compositions of the surface CO_2 flux in the late afternoon only after a deep convective ABL has developed. We suggest that our isotopic large-eddy simulation (ISOLES) model should be a useful tool for testing and formulating research hypotheses on land–air isotopic exchanges.

Electronic supplementary material The online version of this article (doi:10.1007/s10546-011-9631-3) contains supplementary material, which is available to authorized users.

X. Lee (✉) · J. Huang
School of Forestry and Environmental Studies, Yale University, 21 Sachem Street, New Haven, CT 06510, USA
e-mail: xuhui.lee@yale.edu

J. Huang
Yale-NUIST Center on Atmospheric Environment, Nanjing University of Information, Science and Technology, Nanjing, China

J. Huang
I. M. System Group, Environmental Modeling Center, NOAA National Centers for Environmental Prediction, Camp Springs, MD, USA

E. G. Patton
National Center for Atmospheric Research, Boulder, CO, USA

Keywords Isotopes · Keeling plot · Kinetic fractionation · Land-surface model · Large-eddy simulation

1 Introduction

This study concerns the transport, diffusion and surface exchange of the stable isotopes of water vapour and carbon dioxide in the atmospheric boundary layer (ABL). The isotopic species of interest are $C^{18}OO$, $H_2{}^{18}O$ and $^{13}CO_2$, and offer insights into the carbon and water fluxes on land. To date, rich empirical data exist on how biological processes discriminate against the isotopic exchange between plants and the atmosphere (e.g., Yakir and Sternberg 2000); the isotopic flux of $^{13}CO_2$ provides constraints on the atmospheric carbon cycle. In the process of photosynthesis, plants take up the lighter $^{12}CO_2$ molecules more quickly than the heavier $^{13}CO_2$ because of the lower reactivity of $^{13}CO_2$ with rubisco. Additionally, the diffusion of ^{12}C-CO_2 into the stomatal cavity is more efficient due to its higher molecular diffusivity than that of $^{13}CO_2$, a phenomenon known as the kinetic effect. The discrimination against $^{13}CO_2$ by photosynthesis exerts an imprint on atmospheric $^{13}CO_2$ that is uniquely different from the fossil and oceanic signals, allowing atmospheric models to partition ocean, land and anthropogenic carbon fluxes (Ciais et al. 1995; Bush et al. 2007) and inter-annual variability of the land carbon sink (Battle et al. 2000). Furthermore, the respired CO_2 is slightly more enriched than the assimilated CO_2. This isotopic difference holds the promise of allowing the partitioning of the net CO_2 flux into its component fluxes, both globally and in individual ecosystems (Fung et al. 1997; Bowling et al. 2001; Zobitz et al. 2008).

The oxygen isotopes of water and CO_2 ($H_2{}^{18}O$, $C^{18}OO$) are useful tracers for probing the mechanisms that govern the water and carbon fluxes on land. In the process of transpiration, the lighter ^{16}O-H_2O molecules escape more quickly from the stomatal cavity than the heavier $H_2{}^{18}O$ molecules because of the higher saturation vapour pressure (the equilibrium effect) and higher diffusivity of ^{16}O-H_2O (the kinetic effect). This results in a higher ^{18}O content of the leaf water relative to that of the soil water. The enriched leaf ^{18}O-H_2O signal is passed to the CO_2 molecules that diffuse out of the stomatal cavity through a hydration reaction, thus playing an important role in the budget of atmospheric $C^{18}OO$ (e.g., Farquhar et al. 1993). At the ecosystem scale, the transpired water is isotopically different from soil evaporation, allowing the partitioning of the ecosystem water use into its component fluxes (Williams et al. 2004; Lee et al. 2007). Similarly, the $C^{18}OO$ signal can be used to partition the net ecosystem carbon exchange (Ogée et al. 2004; Griffis et al. 2010).

Relatively little is known of the role the ABL flow plays in the isotopic exchange processes. In the ABL, non-linear interactions between the flow and the plant physiological processes may create emergent properties that are not observable at the leaf and plant scales but may be important for regional and global scale studies. For example, although at the leaf scale gaseous exchange through the stomatal opening is a process of molecular diffusion, kinetic fractionation associated with the exchange becomes a wind-dependent property when the vegetation is coupled with the atmosphere (Lee et al. 2009).

Our research represents the first large-eddy simulation (LES) study of $C^{18}OO$, $H_2{}^{18}O$ and $^{13}CO_2$ in the ABL. The primary method deployed is the NCAR's LES model that is dynamically coupled with an isotopic parametrization of land-surface processes. The published modelling studies on these isotopes mostly deal with atmospheric budgets at the regional and global scales (Ciais et al. 1997; Cuntz et al. 2002, 2003) and the exchange processes at the vegetation-atmosphere interface (Riley et al. 2002; Baldocchi and Bowling 2003; Ogée et al. 2003). In an ABL study, Chen et al. (2006) coupled a one-dimensional ensemble ABL model with an isotopic land-surface model (LSM) parametrization to investigate the rectifier effect on atmospheric $^{13}CO_2$. Our LES differs from their ensemble approach in several respects. In the LES domain, the isotopic fluxes respond dynamically to vegetation and microclimatic controls, at the temporal scale of turbulent eddies (seconds), thermal circulation (minutes) and ABL entrainment (hours). Mesoscale motions, either in the form of organized convection structures (Kanda et al. 2004) or thermal circulations locked onto landscape heterogeneity (Kang and Davis 2008), are explicitly resolved. The ABL entrainment is not specified or assumed, but results from the initial conditions and the imposed forcing. The model can distinguish different effects of mesoscale motions on active (heat, water vapour) and passive scalars (the isotopic tracers). In the coupled modelling system, the driving variables of the biosphere–air interactions are themselves interconnected, much as in the real atmosphere, at multiple spatial scales (turbulent eddy scale to the scale of the ABL). The simultaneous simulations of $^{13}CO_2$, $C^{18}OO$ and $H_2{}^{18}O$ allow us to examine the transport and diffusion of the three isotopologues in a consistent manner.

Our study has three specific objectives: the first objective is to investigate the sensitivity of the $C^{18}OO$, $^{13}CO_2$ and $H_2{}^{18}O$ surface fluxes to wind speed in the ABL. In an isotopic LSM study, leaf water in windier conditions is more enriched in $H_2{}^{18}O$ (Xiao et al. 2010), and shows that a 10% reduction in wind speed at the screen height causes a 7% reduction in the ecosystem $C^{18}OO$ isoforcing, primarily through the change in kinetic fractionation of $H_2{}^{18}O$. This sensitivity was obtained by perturbing the wind speed at the reference height above the canopy and keeping other driving variables of the LSM unchanged. In the real world, however, a change in wind speed also alters other screen-height variables, such as relative humidity that exerts a strong influence on the leaf water ^{18}O composition. In the present study, the interplay among the driving variables is accounted for in the LES. This feature allows the wind sensitivity to be examined at a high level of realism that cannot be achieved with an offline LSM simulation.

The second objective is to examine the variations of the atmospheric compositions of these isotopes at scales ranging for turbulent eddies to the diurnal time scale and in the vertical domain extending from the surface to the capping inversion. The published observational studies of these variations are either near-continuous in time but limited to the air layer near the ground (Bowling et al. 2005; Lee et al. 2006; Pataki et al. 2006; Griffis et al. 2010) or span the ABL in the vertical but are discrete in time (He and Smith 1999; Lloyd et al. 2001). The LES modelling results can inform the search of mechanisms underlying the observed patterns and future field experiments using fast-responding isotopic analyzers.

The third objective is to evaluate the accuracy of the Keeling mixing line method for inferring the source CO_2 or H_2O isotopic signal, δ_F, from observed high-frequency time series of their compositions δ_a in air. Bowling et al. (1999) hypothesize that δ_F is equivalent to the intercept coefficient, a, of the following regression equation

$$\delta_a = a + b/c, \tag{1}$$

where c is the mixing ratio of the corresponding major isotopic species, and b is the slope coefficient of the regression. It is now possible to implement this calculation with fast-responding in-situ measurements of δ_a (e. g. Griffis et al. 2008, 2010). Assessment of the accuracy of the method is however challenging because independent information on δ_F is difficult to obtain in field experiments, a difficulty that is circumvented in the LES domain since δ_F is known. In our study we simulate the Keeling method by recording the high-frequency time series of δ_a and c generated by the LES model at every grid point. The intercept coefficient a from the regression analysis is then compared to the known source signal δ_F in the LES domain. A similar approach has been used in LES investigations of bias errors inherent in the eddy-covariance method (Kanda et al. 2004; Steinfeld et al. 2007; Huang et al. 2008).

2 Model Description

2.1 The Isotopic Large-Eddy Simulation Model

2.1.1 Notation of Isotopic Variables

All isotopic variables are expressed in the delta notation in reference to the Vienna Standard Mean Ocean Water (VSMOW) standard for $H_2{}^{18}O$ and Vienna PeeDee Belemnite (VPDB) standard for $C^{18}OO$ and $^{13}CO_2$. Superscripts w, 18 and 13, denote $H_2{}^{18}O$, $C^{18}OO$ and $^{13}CO_2$, respectively, and subscripts a and F denote the $^{18}O/^{16}O$ or $^{13}C/^{12}C$ ratio in air and the isotopic ratio of the surface flux, respectively. For example, δ_a^{18} is the $^{18}O/^{16}O$ ratio of atmospheric CO_2 and δ_F^{13} is the ratio of $^{13}CO_2$ to ^{12}C-CO_2 flux of the surface. The kinetic fractionation factors are denoted by ϵ_k in the unit of ‰ and superscripted appropriately for each of the three isotopologues.

2.1.2 Model Overview

The isotopic LES model (ISOLES) consists of four components (LES dynamics, LES tracer, LSM, and LSM isotope). Figure 1 shows how these components are linked to one another. A standard LSM is driven by the variables u, T_a, vapour pressure deficit or VPD, predicted from the LES calculations of the flow dynamics, at the first grid height. The LSM-predicted fluxes of sensible and latent heat are fed into the LES dynamics to drive the development of the ABL. The LSM code also provides the predictions of those variables necessary for the isotopic LSM parametrization. In parallel with the simulation of wind, pressure and active scalars (heat and water vapour), the LES solves the conservation equations of four passive tracers: the mixing ratio of CO_2, δ_a^w, δ_a^{13} and δ_a^{18}. The lower boundary conditions for the LES tracer calculations are provided by the CO_2 flux and the isoforcing of $H_2{}^{18}O$, $C^{18}OO$ and $^{13}CO_2$, calculated with the standard LSM and its isotopic counterpart, respectively. The LES fields exert a "top-down" influence on the flux and the isoforcing terms by modulating the CO_2 concentration, the ABL isotopic budgets and the kinetic effects. The coupling between the LES and LSM and its isotopic counterpart occurs at every timestep of model integration, which typically varies between 2.8 and 3.2 s.

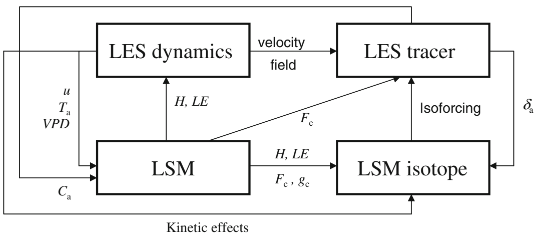

Fig. 1 A box diagram showing the structure of the coupled isotope-LSM–LES modelling system (ISOLES). Variable definitions are: u wind speed, T_a air temperature, *VPD* saturation vapour pressure deficit, C_a CO_2 concentration, H sensible heat flux, LE latent heat flux, F_c CO_2 flux, g_c canopy or surface conductance, δ_a isotopic composition of CO_2 or water vapour in air

These ISOLES components are described elsewhere (Patton et al. 2005; Huang et al. 2009; Xiao et al. 2010); only essential information is summarized below.

2.1.3 The NCAR Large-Eddy Simulation Code

The NCAR's LES, originally described by Moeng (1984) and Sullivan et al. (1998) and subsequently modified by Patton et al. (2005), is used. The surface fluxes of heat, water vapour and trace gases are computed from the LSM coupled with the LES (Huang et al. 2009). The coupled modelling system allows surface fluxes to respond dynamically to the available energy and the ABL feedback on the surface processes. In our study, a routine is embedded in the model to compute intermediate summation terms at all the grid points in the LES domain. These summation terms are saved at hourly intervals for computation of the temporal or Reynolds statistics (Huang et al. 2008) and the Keeling regression coefficients in post-processing analysis. For example, the coefficient a and b in Eq. (1) are determined from the summation terms $\sum \delta_a$, $\sum \delta_a^2$, $\sum 1/c$, $\sum 1/c^2$ and $\sum \delta_a/c$.

2.1.4 LES Tracer Simulation

The conservation equation of CO_2 is solved in the same manner as that of the water vapour mixing ratio. In the coupled code, the CO_2 flux computed from the LSM parametrizations of photosynthesis and soil respiration serves as the lower boundary condition to the equation governing the CO_2 mixing ratio. A system of equations governing the transport and diffusion of $H_2{}^{18}O$, $C^{18}OO$ and $^{13}CO_2$ is integrated into the LES; we note that δ_a^w, δ_a^{13} and δ_a^{18} are conserved quantities. (In the LES cloud formation is not permitted to alter the $H_2{}^{18}O$ composition in vapour.) As with CO_2 or water vapour mixing ratio (Lee and Massman 2011), the material derivative of δ_a is zero in air layers free of sources and sinks,

$$\frac{d\delta_a}{dt} = 0. \tag{2}$$

The expanded form of Eq. (2) is identical in form to the conservation equations of the CO_2 and water vapour mixing ratios, as

$$\frac{\partial \delta_a}{\partial t} + \frac{\partial u\delta_a}{\partial x} + \frac{\partial v\delta_a}{\partial y} + \frac{\partial w\delta_a}{\partial z} = 0, \tag{3}$$

where t is time, and u, v and w are the three velocity components in the x, y and z directions. Manipulation of the resolved-scale quantities and the resulting subfilter scale stress divergence terms is handled identically to that for temperature and humidity. The isotope tracers are transported similarly to heat and vapour at the subfilter scales. At the large scales, their transport results naturally from their respective transport equations, which are solved in the same manner as those of the CO_2 and water vapour mixing ratios but with different surface flux and entrainment boundary conditions. The lower boundary conditions for these equations are specified by an isoforcing term and are calculated by the isotopic LSM, as described below.

2.1.5 Land-Surface Model

The LSM of Ronda et al. (2001) is adopted here, and solves the surface processes and provides the time-dependent surface fluxes driving the ABL evolution. The surface conductance and canopy photosynthesis are derived from a biochemical formulation. The canopy or surface temperature (T_{sk}) is solved from the energy balance equation using a Taylor linear expansion method. The sensible (H) and latent heat fluxes (LE) are determined with the standard aerodynamic formulation. In an offline mode, the model is driven by incident solar radiation, soil moisture, leaf area index (*LAI*) and variables measured at the screen height in the surface layer (air temperature, humidity, CO_2 concentration, wind speed). In the coupled mode, the screen-height variables are simulated by the LES at its first grid level (Huang et al. 2009) and the incoming solar radiation, soil moisture and *LAI* are prescribed. The incoming longwave radiation is parametrized with an Idso-type scheme as a function of air temperature at the first grid level (Idso 1981).

In the simulations reported below, the C_3 photosynthetic pathway is assumed. Soil moisture is specified implicitly in the LSM code by setting the photosynthetic capacity to a fraction of the maximum capacity (parameter f_5, Huang et al. 2009); *LAI* is assigned a value of 4.

2.1.6 Isotopic Land-Surface Model

The flux boundary condition to Eq. (3) is given by the isoforcing expression (in units of $\mathrm{m\,s^{-1}‰}$)

$$I = \frac{F}{C_a}(\delta_F - \delta_a), \tag{4}$$

where F and C_a denote the surface flux and concentration at the first grid height of water vapour or carbon dioxide, respectively. Tans (1980), Cuntz et al. (2003) and others have shown that I is the appropriate flux boundary condition for the isotopic budget in the atmosphere. At the ecosystem scale, I is equivalent to the ecosystem-scale eddy flux of delta, $\overline{w'\delta'_a}$, where the overbar denotes Reynolds averaging, the prime is a departure from the average, and w is the vertical velocity (Lee et al. 2009). This also holds at the local scale of the LES grid.

The isoforcing of $C^{18}OO$ is the sum of a canopy and a soil component (Xiao et al. 2010); the canopy component is parametrized according to a big-leaf version of Farquhar et al. (1993) and Gillon and Yakir (2001). The CO_2 in the leaf chloroplast is in partial equilibrium, assuming a hydration efficiency of 0.95, with the leaf water whose $H_2{}^{18}O$ composition (δ_L^w) is predicted according to the Craig–Gordon model (Craig and Gordon 1965). The soil component assumes that the respired CO_2 originates from a single depth and is in full equilibrium with the soil water at that depth.

The isoforcing of $^{13}CO_2$ also consists of a canopy and a soil component (Lee et al. 2009). The net fractionation due to carboxylation takes an average value of 27‰ for C_3 plants (Farquhar et al. 1989), while the respired soil CO_2 has a ^{13}C composition of −22‰ (Griffis et al. 2007).

Soil evaporation is neglected in the parametrization of the $H_2{}^{18}O$ isoforcing. This omission approximates conditions of a fully-leafed ecosystem where soil evaporation is usually much smaller than transpiration (Black et al. 1996; Wilson et al. 2001; Lee et al. 2007; Griffis et al. 2011) and the associated errors in the surface $H_2{}^{18}O$ isoforcing is on the order of 10%. Applying Eq. (4) to the canopy isoforcing on atmospheric $H_2{}^{18}O$, we have

$$I = \frac{E}{\rho_v}(\delta_x - \delta_a^w) \tag{5}$$

where δ_x is the ^{18}O composition of the xylem water with the same value as the soil water (−5‰). The transpiration flux E is predicted by the LSM and the vapour density ρ_v and $H_2{}^{18}O$ isotopic composition δ_a^w by the LES; Eq. (5) assumes that the canopy transpiration is in isotopic steady state.

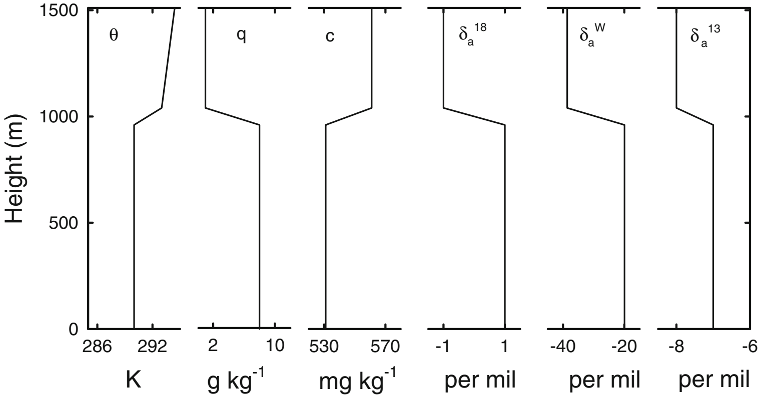

Fig. 2 Initial profiles of potential temperature θ, specific humidity q, CO_2 mixing ratio c, $C^{18}OO$ composition δ_a^{18}, $H_2{}^{18}O$ composition and $^{13}CO_2$ composition used in the snapshot simulations except for the cases noted in the text

One goal of our study is to understand the sensitivity of I, δ_a and δ_L^w to parametrizations of the kinetic effects. At the canopy scale, the kinetic factor for $H_2{}^{18}O$ is a resistance-weighted mean of the molecular, the leaf boundary layer and the turbulent value as,

$$\epsilon_k^w = \frac{21 r_b^w + 32 r_c^w}{r_a + r_b^w + r_c^w} \tag{6}$$

where r_a, r_b^w, r_c^w are the aerodynamic, the leaf boundary-layer, and the canopy resistances to water vapour, respectively. Similar formulations for ϵ_k^{13} and ϵ_k^{18} are given by Lee et al. (2009).

2.2 Model Configurations

2.2.1 Snapshot Simulations

The snapshot simulations are meant to reproduce the ABL flow over a short duration of about 1 h and are initiated with temperature, humidity and CO_2 profiles typical of the mid-afternoon convective conditions at mid-latitudes in summer (Fig. 2). The initial δ_a^w profile is assumed to follow the Rayleigh distillation relationship

$$\delta_{a,o}^w = 8.99 \ln(q_o/0.622) - 42.9 \tag{7}$$

(Lee et al. 2006), where q_o is the initial specific humidity (g kg^{-1}).

The simulations are made with various parameter combinations. The photosynthesis scale factor f_5 is set at three values (0.02, 0.2, 0.9) corresponding to soil moisture regimes near the wilting point, average conditions and near the field capacity, respectively. The surface roughness has values 0.02, 0.1, 0.5 and 1 m, and the geostrophic wind (u_g) is set at 0, 1, 3, and 5 m s^{-1}. To assess the impact of atmospheric humidity on the isotopic exchanges, the simulations are repeated for a moist ABL where the initial q is 16 g kg^{-1} in the mixed layer and 5 g kg^{-1} in the free atmosphere, with the initial δ_a^w adjusted according to Eq. (7). In all, a total of 78 snapshot simulations have been performed. The size of the simulation domain is $6.4 \times 6.4 \times 1.92$ km^3, and grid-spacing 50 m $\times$ 50 m $\times$ 20 m in the x, y and z direction, respectively. The incoming solar radiation is set at 700 W m^{-2}. Processing of the LES data is performed after the turbulent kinetic energy has reached a quasi-steady state, usually after 120 min of integration time (Patton et al. 2005).

2.2.2 Simulations of the Time-Evolving ABL

A time-varying incoming solar radiation, corresponding to a typical summer day in mid-latitudes under clear-sky conditions, is used to drive the dynamic evolution of the ABL (Huang et al. 2011). The Sun rises at 0600 and sets at 1800 solar time (ST), with integration starting at 0415 ST. To avoid the collapse of the LES simulations, we set the solar flux to 130 $W\,m^{-2}$ between 0415 and 0616 ST, resulting in a slightly positive sensible heat flux of 2 $W\,m^{-2}$. The initial profiles are presented in Fig. S3 (online supplement). Briefly, the initial temperature profile is matched with the composite sounding profile collected at sunrise during the 1994 intensive field campaigns in the BOREAS southern study area (Barr and Betts 1997). For a moderately humid ABL, the initial q is 8 $g\,kg^{-1}$ at the ground, decreases linearly to 2 $g\,kg^{-1}$ at a height of 2 km and remains constant at 2 $g\,kg^{-1}$ above 2-km height; this profile represents conditions commonly observed in mid-latitudes (Barr and Betts 1997). For a moist ABL, the corresponding q values are 16, 10 and 10 $g\,kg^{-1}$. The initial CO_2 profile consists of a surface value of 671 $mg\,kg^{-1}$, a large vertical gradient of -2.8 $mg\,kg^{-1}\,m^{-1}$ in the surface layer and a constant value of 570 $mg\,kg^{-1}$ above. The initial δ_a^w is provided by Eq. (7), and the initial δ_a^{13} and δ_a^{18} are set at -8 and -1‰, respectively, at all heights.

The soil moisture parameter f_5 is set to 0.2, surface roughness at 0.5 m, and the geostrophic wind speed at 1 and 5 $m\,s^{-1}$. The domain size and grid spacing are the same as for the snapshot simulations.

3 Sensitivity of Surface Isotopic Exchanges

In this section, the snapshot simulations are used to understand the sensitivity of the surface isotopic properties to wind, humidity and stomatal resistance. These simulations represent midday conditions. One focus is on the abiotic and biotic controls on the leaf water $H_2{}^{18}O$ composition (δ_L^w). We note that δ_L^w is an important parameter for several earth science problems including the Dole effect regarding atmospheric ^{18}O-O_2 (Bender et al. 1994), atmospheric $C^{18}OO$ budget (Ciais et al. 1997) and crop yield prediction (Barbour et al. 2000). The time evolving simulations are used to quantify the wind sensitivity of the ABL on δ_a^w and δ_a^{13} and δ_a^{18}.

3.1 Sensitivity in the Snapshot Simulations

Figure 3 shows how the surface $C^{18}OO$ isoforcing and δ_L^w respond to changes in u_g. To aid the interpretation, several intermediate variables are also shown. Increasing u_g from 0 to 5 $m\,s^{-1}$ raises δ_L^w by 1.2‰, giving a sensitivity of 0.23 ‰/($m\,s^{-1}$) (Fig. 3d). As wind speed increases, the transfer of water vapour becomes more restricted by molecular diffusion through the stomata than by turbulent diffusion in the surface layer, resulting in a higher ϵ_k^w (Fig. 3b; Lee et al. 2009). This wind effect is offset somewhat by the indirect effect associated with the change in relative humidity (*RH*). Here *RH* is defined as the ratio of the vapour pressure at the first grid level to the saturation pressure at the surface temperature (T_{sk}). Increasing u_g causes the surface to cool (Fig. 3a) and *RH* to rise (from 34% at $u_g = 0$ to 38% at 5 $m\,s^{-1}$). The Craig–Gordon model predicts a sensitivity of -0.4‰ per % *RH* change (Still et al. 2009).

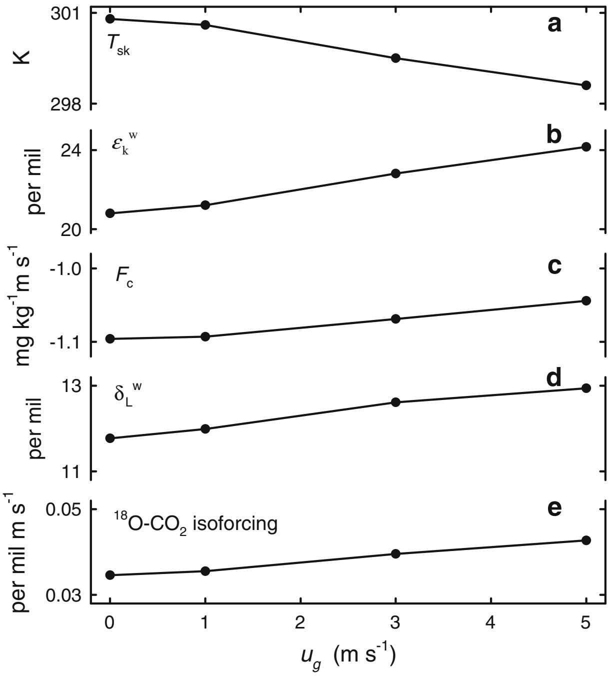

Fig. 3 Sensitivity of surface variables to the geostrophic wind ($z_o = 0.5$, $f_5 = 0.2$, $q = 8\,g\,kg^{-1}$): (*a*) surface skin temperature (T_{sk}); (*b*) kinetic factor for $H_2{}^{18}O$ (ϵ_k^w); (*c*) surface CO_2 flux (F_c); (*d*) leaf $H_2{}^{18}O$ composition (δ_L^w); (*e*) surface $C^{18}OO$ isoforcing

The relative strength of the kinetic effect and the indirect *RH* effect on δ_L^w appear to depend on ambient humidity. Under the same conditions as in Fig. 3 but with the ABL specific humidity doubled to $16\,g\,kg^{-1}$, a $5\,m\,s^{-1}$ increase in u_g actually reduces δ_L^w by approximately 0.4‰. Such high humidity conditions are not common in mid-latitudes.

The sensitivity of isoforcing to wind differs among the three isotopologues. The ISOLES model predicts that the $C^{18}OO$ isoforcing should increase with increasing u_g under the conditions specified in Fig. 2 (Fig. 3e); the wind sensitivity is approximately $1.6 \times 10^{-3}\,m\,s^{-1}‰/(m\,s^{-1})$. In comparison, a stand-alone isotopic LSM simulation gives a higher sensitivity of $6.7 \times 10^{-3}\,m\,s^{-1}‰/(m\,s^{-1})$ (Xiao et al. 2010). Much of the increase is caused by the increase in the $C^{18}OO$ composition of the chloroplast CO_2 through the hydration reaction with the enriched leaf water. A slight increase in the $C^{18}OO$ kinetic fractionation factor ϵ_k^{18}, by 0.7‰ over the 0–5 $m\,s^{-1}$ range, also contributes to the increase in the isoforcing. The positive sensitivity to wind speed occurs despite the reduction in the magnitude of the simulated CO_2 flux F_c (Fig. 3c), recalling that the isoforcing is proportional to F_c (Eq. 4). The reduction in F_c is caused by T_{sk} moving away from the optimum temperature specified by the LSM for photosynthesis. Neither the $H_2{}^{18}O$ nor the $^{13}CO_2$ isoforcing is sensitive to u_g, changing by less than 3% over the 0–5 $m\,s^{-1}$ range (data not shown).

Figure 4 compares the modelled and observed dependence of δ_L^w on *RH* and the kinetic fractionation factor for a surface roughness of 0.1 m. The observations were made in a soybean field near midday with the seasonal mean xylem $H_2{}^{18}O$ composition of −6.9‰ (Welp et al. 2008). The ISOLES model has reproduced the observed negative correlation. The modelled *RH* sensitivity ($-0.32‰/\%RH$) is slightly higher in magnitude than the observed

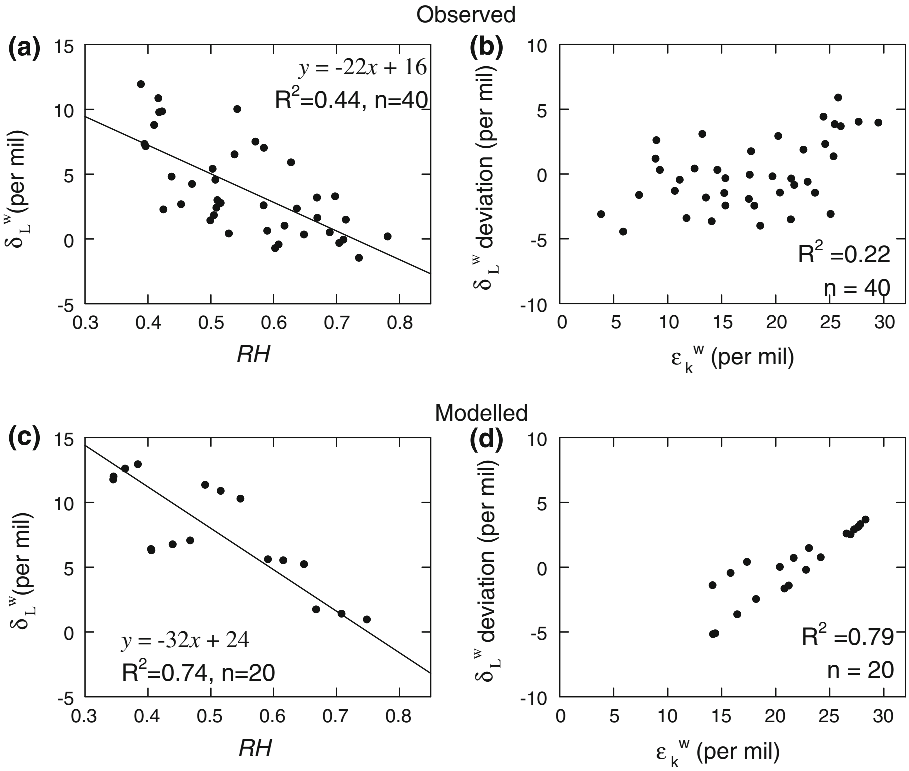

Fig. 4 Comparison of observed (**a**, **b**) and modelled (**c**, **d**) dependence of the leaf $H_2{}^{18}O$ composition (δ_L^w) on relative humidity (*RH*) and the kinetic factor (ϵ_k^w). *Left panels* show the dependence on *RH*, with the line representing the best-fit linear regression. *Right panels* show the deviation of δ_L^w from the regression line as a function of ϵ_k^w. The xylem water $H_2{}^{18}O$ composition is set at −5.0‰ in the simulations and has an averaged value of −6.9‰ in the field observations

value (−0.22‰/%RH). The theoretical analysis of Still et al. (2009) reveals a sensitivity of −0.4‰/%RH. Both the modelled and observed results show that the deviation of δ_L^w from the $\delta_L^w - RH$ regression is related to variations in ϵ_k^w (Fig. 4b, d): ϵ_k^w explains 22% in the observed and 79% in the modelled δ_L^w residuals of the *RH* regression.

Results for other roughness values, given in Fig. S1 of the online supplement, show a tighter control on δ_L^w by *RH* for aerodynamically rougher vegetation. The linear correlation between *RH* and δ_L^w is −0.73 for roughness z_o of 0.02 m and changes to −0.97 for $z_o = 1$ m. The *RH* sensitivity varies between −0.28‰ per %*RH* for $z_o = 0.02$ m and −0.35‰ per %*RH* for $z_o = 1$ m.

The relative roles of biotic (r_c^w) and abiotic (*RH*, z_o, u_g) factors on δ_L^w are illustrated in Fig. 5, which includes the results of all the snapshot simulations. Barbour et al. (2000) found that δ_L^w is positively correlated with the stomatal resistance for eight cultivars of spring wheat. Our simulations suggest that this correlation may also hold across different functional types. In Fig. 5, the canopy resistance r_c^w explains 61% of the variations in δ_L^w, with the remaining variations caused by abiotic factors (*RH*, u_g, z_o) According to Eq. (6), either a reduction in the aerodynamic resistance r_a (as caused by a wind speed or z_o increase) or an increase in r_c^w will raise ϵ_k^w, which in turn will increase δ_L^w.

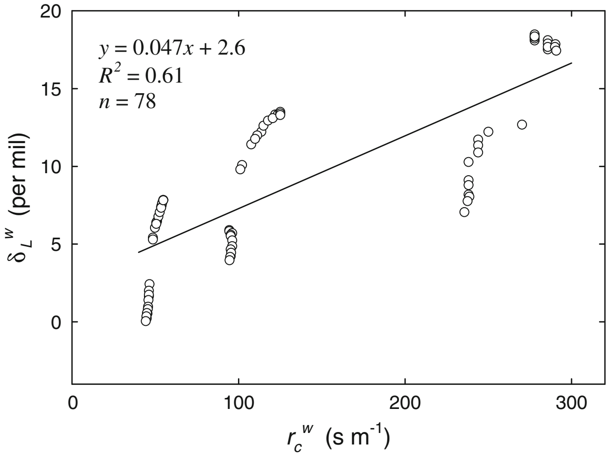

Fig. 5 Modelled leaf $H_2{}^{18}O$ composition (δ_L^w) against the canopy resistance r_c^w for all snapshot simulations. *Solid line* represents the linear regression

Table 1 Sensitivity analysis of the isotopic compositions in five time-evolving ABL simulations

Case	u_g (m s^{-1})	q_o (g kg^{-1})	δ_a^{18}	δ_a^w (‰)	δ_a^{13}
A	5	8	−0.14	−22.08	−7.38
B	1	8	−0.22	−22.04	−7.37
C[a]	5	8	0.02	−22.09	−7.38
D	5	16	−0.49	−15.41	−7.38
E	1	16	−0.47	−15.30	−7.37

The $C^{18}OO$ and $^{13}CO_2$ compositions of atmospheric CO_2 and the $H_2{}^{18}O$ composition of water vapour are for the 500 m height above the ground at 1615 ST. Here q_o is the initial surface specific humidity. All the simulations have the same initial δ_a^{18} and δ_a^{13}

[a] The kinetic factors are set to the molecular values ($\epsilon_k^w = 32$, $\epsilon_k^{18} = 8.8$ and $\epsilon_k^{13} = 4.4$‰)

3.2 Sensitivity in the Time-Evolving Simulations

Table 1 summarizes the mid-ABL isotopic compositions at 1615 ST in five time-evolving ABL cases. Cases A, B, D and E represent four combinations of air humidity and wind speed, and in case C, all the kinetic factors are set to their constant molecular values. Changes in δ_a^{13} and δ_a^w, due to changes in either wind speed or the kinetic formulation, is within the margin of computational errors. For a moderate surface q of 8 g kg^{-1}, the mid-afternoon δ_a^{18} value is increased by 0.08‰ if wind speed changes from 1 to 5 m s^{-1}. The kinetic fractionation formulation has a larger effect, increasing δ_a^{18} by 0.17‰ if turbulent diffusion is ignored.

The 0.08‰ difference between the two wind speeds represents the δ_a^{18} sensitivity to short-term wind perturbations. The cumulative long-term effect would be much larger. The difference in the surface isoforcing (ΔI) is 0.006 ‰ m s^{-1} between the two wind speeds. As an order-of-magnitude estimate, if the wind increase is sustained over 1 month and other conditions remain constant, the mean tropospheric δ_a^{18} will rise by 0.6‰ according to the one-dimensional rate equation

$$\frac{\partial \delta}{\partial t} = \frac{1}{h}(\Delta I) \tag{8}$$

where the tropospheric height h is set at 10 km in this calculation. For comparison, the seasonal amplitude of δ_a^{18} is about 1‰ at Mauna Loa observed by the NOAA flask network.

Table 1 also shows the sensitivity to air humidity. High humidity is usually associated with high δ_a^w (Lee et al. 2006; Wen et al. 2010). This association is prescribed in ISOLES by using a profile of high δ_a^w value to initiate the model simulation (Eq. 7). The δ_a^w sensitivity in Table 1 is caused primarily by a change in the initial condition rather than by a change in the surface isoforcing. In the case of $^{13}CO_2$ and $C^{18}OO$, the sensitivity is caused by changes in both the surface isoforcing and the ABL depth. In the moist case, the ABL is 200 m deeper at 1615 ST than in the moderate humidity case because of a larger surface sensible heat flux (Figs. S2–S5, online supplement). The deepened ABL has the effect of canceling out the enrichment effect of the enhanced surface $^{13}CO_2$ isoforcing, resulting in δ_a^{13} being insensitive to humidity. A deepened ABL, along with a reduced $C^{18}OO$ surface isoforcing, acts to deplete the ABL air in $C^{18}OO$. The overall difference in δ_a^{18} between the two simulations is 0.35‰ at $u_g = 5\ \mathrm{m\,s^{-1}}$. These results suggest that the ABL $C^{18}OO$ composition is more sensitive to humidity perturbations than to wind perturbations.

4 Isotopic Budgets in the ABL

The time evolutions of δ_a^w, δ_a^{13} and δ_a^{18} in the ABL are controlled by the isoforcing at the surface, the exchange through entrainment at the ABL top, and the ABL growth and decay. In this section, we examine these drivers with the time evolving ISOLES simulations.

Figure 6 shows the time evolutions of the hourly mean surface isoforcing averaged over the model domain. All the isoforcing terms are positive during the simulation period of 0700–1600 ST, acting to enrich the ABL air in the three isotopic species. That the timing of the isoforcing peaks coincides with the peak incoming solar radiation can be understood through Eqs. (4) and (5) showing that the isoforcing is in proportion to the flux of CO_2 or water vapour. The midday $C^{18}OO$ isoforcing is about 0.04–0.05 ‰ $\mathrm{m\,s^{-1}}$, which is roughly twice the seasonal mean values observed over a soybean canopy (Lee et al. 2009). The discrepancy may be caused by a potentially very low ^{18}O hydration efficiency in the soybean leaves (Xiao et al. 2010). The modelled midday $^{13}CO_2$ isoforcing (0.025–0.035 ‰ $\mathrm{m\,s^{-1}}$) is in good agreement with the observations of Lee et al. (2009) and Griffis et al. (2010) and with values suggested by the ^{13}C modelling studies of Baldocchi and Bowling (2003), Ogée et al. (2004), and Chen et al. (2006). Our midday $H_2{}^{18}O$ isoforcing is in the range 0.05–0.2 ‰ $\mathrm{m\,s^{-1}}$, in good agreement with the values observed by Farquhar and Cernusak (2005), Lee et al. (2007), Welp et al. (2008) and Griffis et al. (2010). These results demonstrate that the ISOLES model has achieved a reasonable degree of realism.

The impact of humidity differs among the three isotope species (Fig. 6). A large reduction occurs to the $H_2{}^{18}O$ isoforcing in response to the change of the near-surface q from 8 to 16 $\mathrm{g\,kg^{-1}}$. This response is explained by the fact that the $H_2{}^{18}O$ isoforcing is inversely proportional to humidity (Eq. 5). High air humidity reduces the photosynthetic discrimination of $C^{18}OO$ and increases that of $^{13}CO_2$, contributing to the reduction of the $C^{18}OO$ isoforcing and the increase in the $^{13}CO_2$ isoforcing. These results further confirm that the negative correlation between humidity and the $C^{18}OO$ isoforcing is an emergent phenomenon at the ecosystem scale (Xiao et al. 2010).

The flux profiles (Fig. S2, online supplement) depict how the isoforcing terms vary with time, height and the fluxes of buoyancy, specific humidity and CO_2 mixing ratio in the ABL. These terms are computed as the sum of the contributions of the resolved and the subgrid eddies. The resolved eddy contribution is $\langle w''\delta_a''\rangle$, where $\langle\rangle$ denotes the spatial averaging

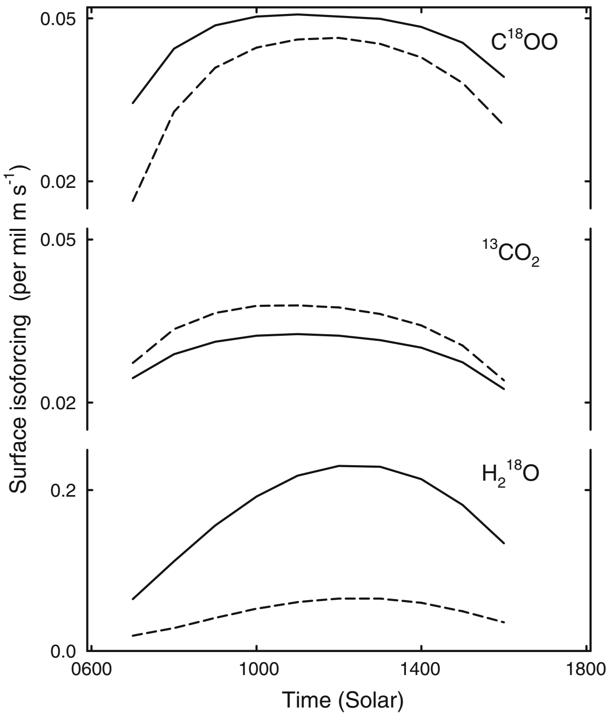

Fig. 6 Surface isoforcing on the atmosphere in two time-evolving ABLs ($z_o = 0.5\,\mathrm{m}$, $u_g = 5\,\mathrm{m\,s^{-1}}$): *solid line* initial surface $q = 8\,\mathrm{g\,kg^{-1}}$; *dashed line* initial surface $q = 16\,\mathrm{g\,kg^{-1}}$

operation, w is the resolved vertical velocity and $''$ is the departure from the spatial mean. As z approaches zero, the computed isoforcing values converge to the surface values parametrized according to Eq. (4). The wiggles in the 0415 ST flux profiles are indicative of the under-resolved nature of the flow field at that time. After turbulence has fully developed, most of the flux profiles display a linear dependence on height, indicating that the ABL is in quasi-steady state despite the time-varying forcing at the surface. The entrainment isoforcing, found at the height of the inflexion point of the flux profile, is quite large, equaling or exceeding the surface values in the morning. The large entrainment values seem to be a robust feature of the ISOLES model as they are seen in other time-varying simulations initiated with various q values.

Also included in the online supplement is the time evolution of the simulated scalar profiles (Fig. S3). The profiles at 0414 ST are essentially the same as the initial profiles. The ABL growth is driven by the surface buoyancy flux and is not affected by the exchange of the passive scalars (CO_2, $C^{18}OO$, $H_2{}^{18}O$, and $^{13}CO_2$). At 1615 ST the ABL has grown to a height of roughly 1600 m, with the growth rate agreeing with the observations made during the BOREAS (Boreal Ecosystem-Atmosphere Study) field campaign (Huang et al. 2011). Other studies have shown slower growths due to a smaller surface buoyancy flux and the influence of large-scale subsidence (Lloyd et al. 2001; Górska et al. 2008) that is not considered in our simulations.

The ABL isotopic enrichment relative to the free atmosphere varies among the three isotope species. Well-mixed δ_a^w, δ_a^{13} and δ_a^{18} profiles have become established after 1100 ST, and at 1615 ST the mid-ABL air is more enriched than the free atmosphere in $C^{18}OO$ by 0.8, $^{13}CO_2$ by 0.6 and $H_2{}^{18}O$ by 8‰. No δ_a^{18} profile observation is available for comparison.

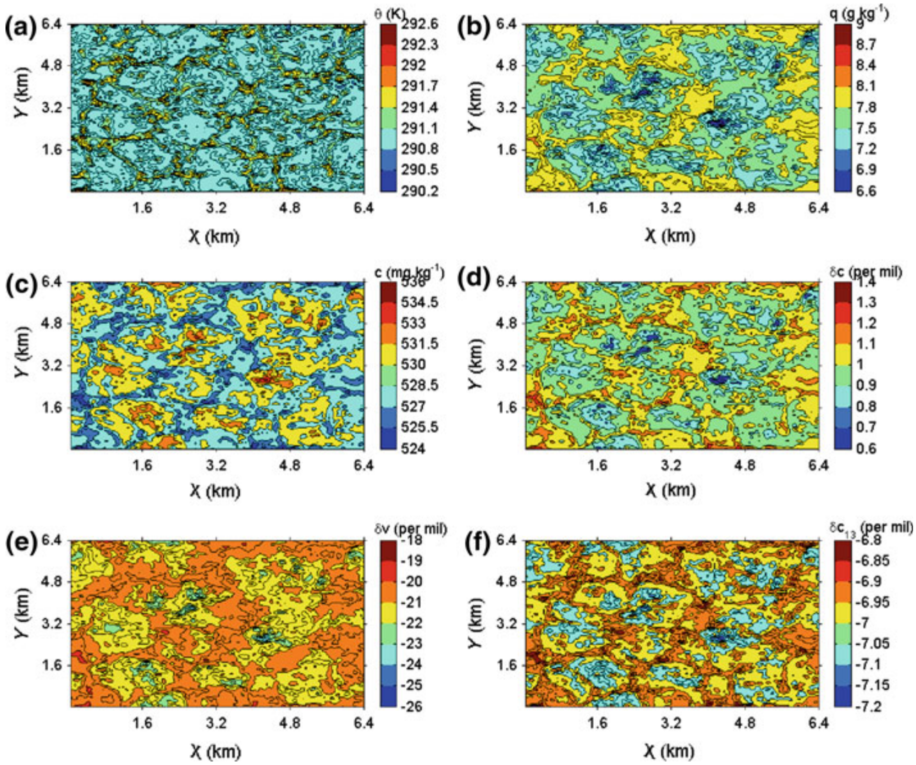

Fig. 7 Contours plots of the instantaneous scalar fields at 100 m above the ground in a snapshot simulation ($z_o = 0.5\,\text{m}, u_g = 0, f_5 = 0.2$): potential temperature (**a**), specific humidity (**b**), CO_2 mixing ratio (**c**) and isotopic compositions of $C^{18}OO$ (**d**), $H_2{}^{18}O$ (**e**) and $^{13}CO_2$ (**f**)

The δ_a^{13} enrichment value is in good agreement with the observations over Siberia (Lloyd et al. 2001), and is higher than the enrichment (0.1–0.3‰) modelled by Chen et al. (2005) for the boreal landscape in Canada. The observed δ_a^{w} enrichment is in the range of 2–25‰ over southern New England, USA (He and Smith 1999). In field campaigns, instruments of much higher precision are needed to resolve the variability in δ_a^{13} and δ_a^{18} than in δ_a^{w}.

The large δ_a^{w} gradient across the capping inversion maintains a strong entrainment isoforcing on the ABL air (Fig. S2e). Its influence is felt all the way down to the surface layer, causing the surface-layer δ_a^{w} to decrease gradually through time (Fig. S3e) despite the large positive surface isoforcing (Fig. 6). Low δ_a^{w} values in the afternoon hours are frequently observed in field campaigns (Helliker et al. 2002; Lai et al. 2005; Lee et al. 2006; Wen et al. 2010). The large $H_2{}^{18}O$ entrainment also contributes to a much more variable δ_a^{w} than δ_a^{13} and δ_a^{18} at the turbulent time scales (Figs. 7, S4).

5 Turbulent Fluctuations of the Isotopic Compositions

Figure 7 shows an example of the horizontal variations of the instantaneous scalar fields at $z = 100$ m above the ground in a snapshot ISOLES simulation. Not surprisingly, the classic turbulent organized structures are seen in the three δ quantities. The δ_a^{w} field is less coherent and more variable than the δ_a^{13} and δ_a^{18} fields, which is indicative of a stronger entrainment influence on δ_a^w in the deep convective boundary layer. The peak-to-peak variations (8‰ in δ_a^w, 0.5‰ in δ_a^{13} and 0.8‰ in δ_a^{18}) are in approximate proportion to their respective jump values across the capping inversion (Fig. 2). At a given grid, δ_a^w shows temporal fluctuations that are one order of magnitude greater than those of δ_a^{13} and δ_a^{18} (Fig. S6, online supplement).

6 Keeling Mixing Line Analysis

Figure 8 top panel compares the Keeling intercept with the true isotopic composition of the surface flux of water vapour δ_F^w. To simplify the comparison, we make the assumption of isotopic steady state so that δ_F^w is identical to the value of −5‰ prescribed for the xylem water. The Keeling intercept is first determined with the geometric mean regression using the ISOLES turbulent time series of δ_a^w and q for every grid point and then averaged across the simulation domain. The Keeling intercept is biased low except at 0800 ST, with a maximum bias error of −2.5‰.

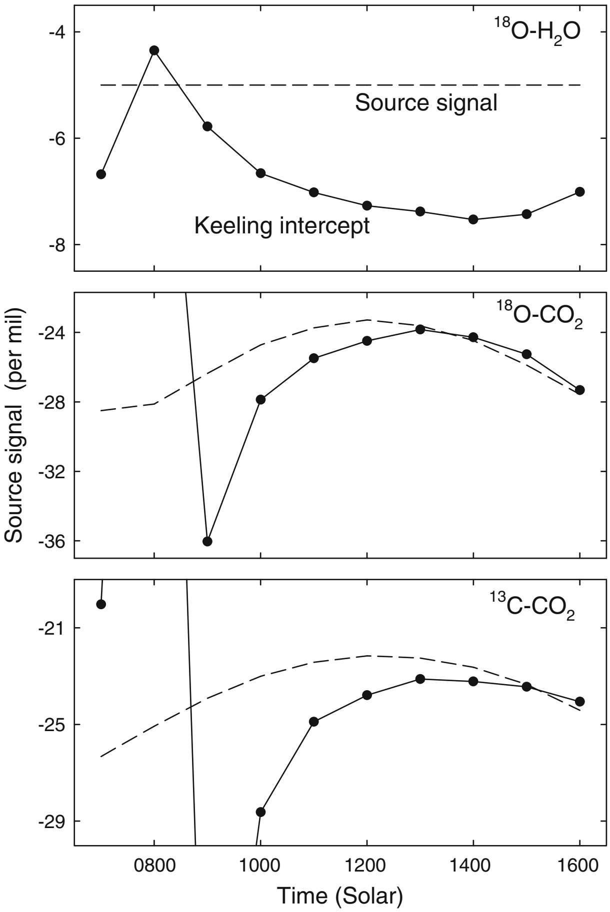

Fig. 8 Comparison of the Keeling intercepts with the true source signals of the surface fluxes ($z_o = 0.5\,\mathrm{m}, u_g = 5\,\mathrm{m\,s^{-1}}$)

Table 2 Impact of entrainment on the Keeling intercept (a, ‰)

Isotope	$H_2{}^{18}O$	$^{13}CO_2$	$C^{18}OO$
δ_F	−5.0	−25.4	−27.9
a with entrainment	−3.0	−29.2	−29.9
a without entrainment	−5.5	−25.1	−27.8

The Keeling intercept is computed with the ISOLES Reynolds time series at a height of 60 m above the ground. The initial profiles either contain large gradients at the capping inversion (with entrainment) or are invariant with height (with no entrainment). The true isotopic signals of the surface source (δ_F, ‰) are also given

A similar comparison is presented in Fig. 8 middle and bottom panels for CO_2. In this model run, the soil respiration flux has been set to zero, so that the only source term is photosynthesis whose isotope signals δ_F^{13} and δ_F^{18} are calculated by the isotopic LSM code embedded in ISOLES. The Keeling intercepts are noisy before 1000 ST, are biased low by 1.2–3.2‰ for $C^{18}OO$ and 1.6–5.6‰ for $^{13}CO_2$ between 1000 and 1200, and reaches reasonable agreement with the true signals in the later afternoon hours (1500–1600 ST).

We postulate that entrainment is the main reason for the bias errors of the Keeling analysis. (Early morning turbulence is also under-resolved.) Entrainment is a process by which the non-turbulent free-tropospheric air is mixed into the turbulent ABL. Driven by the gradient of the scalar field across the capping inversion, it plays a large role in the ABL budgets of heat, water vapour, and carbon dioxide (Barr and Betts 1997; Sullivan et al. 1998; Betts et al. 2004; Helliker et al. 2004; Lai et al. 2006). Entrainment also transports into the ABL air that is more depleted in $C^{18}OO$, $^{13}CO_2$ and $H_2{}^{18}O$ (Fig. S3, online supplement). The Keeling analysis is unambiguous if diffusion is linked to a single source, but in the convective ABL, diffusion results from both the surface and the entrainment sources. In other words, the problem is that of dual-source diffusion (Moeng and Wyngaard 1984).

The above explanation is supported by the results of two snapshot simulations (Table 2). In the first simulation, the entrainment influence is maintained by sharp gradients in the initial profiles at the capping inversion, as shown in Fig. 2. In the second simulation, the initial profiles of all the scalars except temperature are constant throughout the model domain (Huang et al. 2008). For the first simulation, the Keeling intercepts deviate from the true source signals by more than 2‰; for the second simulation, an agreement better than 0.5‰ is achieved. The small errors of the second simulation have to do with the fact that the entrainment fluxes cannot be completely avoided in snapshot large-eddy simulations. Even though the initial profiles were constant with height, by the time the field of the turbulent kinetic energy reached quasi-steady state, small gradients in these scalars have developed across the capping inversion. Moeng and Wyngaard (1984) and Patton et al. (2003) show that the diffusion of a bottom-up tracer is always affected by entrainment and is therefore never truly a bottom-up process.

That entrainment can extend its influence all the way down to the surface layer is evident in the less-than-perfect correlation between the temperature and humidity turbulent time series (Roth and Oke 1995; Katul et al. 2008; Scanlon and Kustas 2010). Entrainment does not necessarily weaken the correlation between the (inverse of) scalar mixing ratio and its isotopic composition because the entrainment scalar flux and isoforcing are in the same direction as their surface counterparts. However, entertainment alters the intercept and the slope parameters of the Keeling linear regression. Our results suggest that the Keeling method is, in general, not reliable for $H_2{}^{18}O$ and may be a reasonable approximation to δ_F^{13} and δ_F^{18} in the late afternoon only after a deep convective ABL has developed.

7 Conclusions

In this study, we have developed an isotopic LES model (ISOLES) for simulating δ_a^w, δ_a^{13} and δ_a^{18} in the ABL. The model is an extension of the NCAR's LES and consists of four fully interactive components that simulate the dynamics of the ABL flow, the transport and diffusion of these isotopic tracers, a LSM coupled to the ABL flow and an isotopic LSM that supplies the surface flux boundary conditions for the tracer simulation. An online scheme is embedded in the model to calculate, at every grid point, the temporal or Reynolds statistics of the turbulent time series of the CO_2 and H_2O mixing ratios and their isotopic compositions.

The ISOLES simulations confirm previous findings that the ^{18}O composition of leaf water δ_L^w is sensitive to relative humidity and wind speed in the ABL. This relationship is partly imposed on the system by the isotopic LSM parametrization and by the interactive nature of the driving variables (Fig. 1). The modelled sensitivity to *RH* is -0.28 to $-0.35‰/(\%RH)$ and the sensitivity to the geostrophic wind (u_g) is about $0.23‰/(\mathrm{m\,s^{-1}})$. The $C^{18}OO$ composition of the ABL air is moderately sensitive to u_g, increasing by 0.008‰ per $\mathrm{m\,s^{-1}}$ as u_g increases from 0 to 5 $\mathrm{m\,s^{-1}}$; this wind sensitivity is higher than if the isotopic LSM is run in offline mode without being coupled to the ABL flow where only wind speed is perturbed. The ABL values of δ_a^w and δ_a^{13} are not sensitive to u_g.

The temporal evolutions and vertical patterns of δ_a^w, δ_a^{13} and δ_a^{18} in the ABL are controlled by their respective surface isoforcing and isoforcing at the entrainment layer. The temporal and spatial variations in δ_a^w at the turbulent eddy scales are one order of magnitude greater than the variations in δ_a^{13} and δ_a^{18}. In a fully-developed convective ABL, δ_a^w, δ_a^{13} and δ_a^{18} are well mixed as with other conserved atmospheric quantities; the mid-ABL air is more enriched than the free atmosphere, with the enrichment value an order of magnitude greater in $H_2{}^{18}O$ (8‰) than in $C^{18}OO$ and $^{13}CO_2$ (<0.8‰). In field campaigns, instruments of much higher precision are needed to resolve the variability in δ_a^{13} and δ_a^{18} than in δ_a^w.

The ISOLES model is a useful tool for testing and formulating research hypotheses. For example, the turbulent time series simulated by the model are used to compute the Keeling intercepts, with the results showing that the Keeling method does not give a reliable estimate of the $H_2{}^{18}O$ composition of the surface water vapour flux and may be a reasonable approximation to the $^{13}CO_2$ and $C^{18}OO$ compositions of the surface CO_2 flux in the late afternoon only after a deep convective ABL has developed. This assessment is restricted to the time series of eddy scales (<seconds) under the conditions specified for the model simulations and does not apply to other types of Keeling applications, such as in analyzing the relationships between the CO_2 mixing ratio and its isotopic composition observed in a vertical profile in the surface layer or observed through the course of the night inside a forest.

Acknowledgments This research was supported by the U.S. National Science Foundation through grant ATM-0914473. This research used resources of the National Energy Research Scientific Computing Center, which is supported by the Office of Science of the U.S. Department of Energy under Contract No. DE-AC02-05CH11231. The National Center for Atmospheric Research is sponsored in part by the National Science Foundation. The authors thank an anonymous reviewer whose careful comments helped improve the paper.

References

Baldocchi DD, Bowling DR (2003) Modeling the discrimination of $^{13}CO_2$ above and within a temperate broad-leaved forest canopy on hourly to seasonal time scales. Plant Cell Environ 26:231–244

Barbour MM, Fischer RA, Sayre KD, Farquhar GD (2000) Oxygen isotope ratio of leaf and grain material correlates with stomatal conductance and grain yield in irrigated wheat. Aust J Plant Physiol 27:625–637

Barr A, Betts A (1997) Radiosonde boundary layer budgets above a boreal forest. J Geophys Res 102:29205–29212

Battle M, Bender ML, Tans PP, White JWC, Ellis JT, Convay T, Francey RJ (2000) Global carbon sinks and their variability inferred from atmospheric O_2 and ^{13}C. Science 287:2467–2470

Bender M, Sowers T, Labeyrie L (1994) The Dole effect and its variations during the last 130000 years as measured in the Vostok ice core. Glob Biogeochem Cycles 8:363–367

Betts AK, Helliker B, Berry J (2004) Coupling between CO_2, water vapour, temperature, and radon and their fluxes in an idealized equilibrium boundary layer over land. J Geophys Res 109:D18103. doi:10.1029/2003JD004420

Black TA, den Hartog G, Neumann HH, Blanken PD, Yang PC, Russell C, Nesic Z, Lee X, Chen SG, Staebler R, Novak MD (1996) Annual cycles of water vapor and carbon dioxide fluxes in and above a boreal aspen forest. Glob Chang Biol 2:219–229

Bowling DR, Baldocchi DD, Monson RK (1999) Dynamics of isotopic exchange of carbon dioxide in a Tennessee deciduous forest. Glob Biogeochem Cycles 13:903–922

Bowling DR, Tans PP, Monson RK (2001) Partitioning net ecosystem carbon exchange with isotopic fluxes of CO_2. Glob Chang Biol 7:127–145

Bowling DR, Burns SP, Conway TJ et al (2005) Extensive observations of CO_2 carbon isotope content in and above a high-elevation subalpine forest. Glob Biogeochem Cycles 19:GB3023

Bush SE, Pataki DE, Ehleringer JR (2007) Sources of variation in $\delta^{13}C$ of fossil fuel emissions in Salt Lake City, USA. Appl Geochem 22:715–723

Chen B, Chen JM, Tans PP, Huang L (2006) Simulating dynamics of ^{13}C of CO_2 in the planetary boundary layer over a boreal forest region: covariation between surface fluxes and atmospheric mixing. Tellus 58B:537–549

Ciais P, Tans PP, Trolier M et al (1995) A large northern hemisphere terrestrial CO_2 sink indicated by $^{13}C/^{12}C$ ratio of atmospheric CO_2. Science 269:1098–1102

Ciais P, Denning AS, Tans PP, Berry JA, Randall DA, Collatz GJ, Sellers PJ, White JWC, Trolier M, Meijer HAJ, Francey RJ, Monfray MH (1997) A three-dimensional synthesis study of $\delta^{18}O$ in atmospheric CO_2: 1. Surface fluxes. J Geophys Res 102:5857–5872

Craig H, Gordon LI (1965) Deuterium and oxygen-18 variations in the ocean and the marine atmosphere. In: Tongiorgi E (ed) Stable isotopes in oceanographic studies and paleotemperatures. Lab di Geol Necl, Pisa, pp 9130

Cuntz M, Ciais P, Hoffmann G (2002) Modeling the continental effect of oxygen isotopes over Eurasia. Tellus B 54:895–909

Cuntz M, Ciais P, Hoffmann G, Knorr W (2003) A comprehensive global three-dimensional model of ^{18}O in atmospheric CO_2: 1 validation of surface processes. J Geophys Res 108:4527

Farquhar GD, Cernusak LA (2005) On the isotopic composition of leaf water in the non-steady state. Funct Plant Biol 32:293–303

Farquhar GD, Ehleringer JR, Hubick KT (1989) Carbon isotope discrimination and photosynthesis. Annu Rev Plant Physiol Plant Mol Biol 40:503–537

Farquhar GD, Lloyd J, Taylor JA, Flanagan LB, Syvertsen JP, Hubick KT, Wong SC, Ehleringer JR (1993) Vegetation effects on the isotope composition of oxygen in atmospheric CO_2. Nature 363:439–443

Fung I, Field CB, Berry JA, Thompson MV et al (1997) Carbon-13 exchanges between the atmosphere and biosphere. Glob Biogeochem Cycles 11:507–533

Gillon J, Yakir D (2001) Anhydrase activity in terrestrial vegetation on the ^{18}O content of atmospheric CO_2. Science 291:2584–2587

Górska M, de Arellano JV, Lemone MA, Heerwaarden CCV (2008) Mean and flux horizontal variability of virtual potential temperature, moisture, and carbon dioxide: aircraft observations and LES study. Mon Weather Rev 136:4435–4451

Griffis TJ, Zhang J, Baker JM, Kljun N, Billmark K (2007) Determining carbon isotope signatures from micrometeorological measurements: implications for studying biosphere–atmosphere exchange processes. Boundary-Layer Meteorol 123:295–316

Griffis TJ, Sargent SD, Baker JM, Lee X, Tanner BD, Greene J, Swiatek E, Billmark K (2008) Direct measurement of biosphere–atmosphere isotopic CO_2 exchange using the eddy covariance technique. J Geophys Res 113:D08304. doi:10.1029/2007JD009297

Griffis TJ, Sargent SD, Lee X, Baker JM, Greene J, Erickson M, Zhang X, Billmark K, Schultz N, Xiao W, Hu N (2010) Determining the oxygen isotope composition of evapotranspiration using eddy covariance. Boundary-Layer Meteorol 137:307–326

Griffis TJ, Lee X, Baker JM, Billmark K, Schultz N, Erickson M, Zhang X, Fassbinder J, Xiao W, Hu N (2011) Oxygen isotope composition of evapotranspiration and its relation to C4 photosynthetic discrimination. J Geophys Res Biogeosci 116:G01035. doi:10.1029/2010JG001514

He H, Smith RB (1999) Stable isotope composition of water vapor in the atmospheric boundary layer above the forests of New England. J Geophys Res 104:11657–11673

Helliker BR, Roden JS, Cook C, Ehleringer JR (2002) A rapid and precise method for sampling and determining the oxygen isotope ratio of atmospheric water vapor. Rapid Commun Mass Spectrom 16:929–932

Helliker BR, Berry JA, Betts AK, Bakwin PS, Davis KJ, Denning AS, Ehleringer JR, Miller JB, Butler MP, Ricciuto DM (2004) Estimates of net CO_2 flux by application of equilibrium boundary layer concepts to CO_2 and water vapor measurements from a tall tower. J Geophys Res 109:D20106. doi:10.1029/2004JD004532

Huang J, Lee X, Patton EG (2008) A modeling study of flux imbalance and the influence of entrainment in the convective boundary layer. Boundary-Layer Meteorol 27:273–292

Huang J, Lee X, Patton E (2009) Dissimilarity of scalar transport in the convective boundary layer in inhomogeneous landscapes. Boundary-Layer Meteorol 130:327–345

Huang J, Lee X, Patton EG (2011) Entrainment and budget of heat, water vapor and carbon dioxide in a convective boundary layer driven by time-varying solar radiation. J Geophy Res Atmos 116:D06308. doi:10.1029/2010/JD014938

Idso SB (1981) A set of equations for full spectrum and 8- to 14-μm and 10.5- to 12.5-μm thermal radiation from cloudless skies. Water Resour Res 17:295–304. doi:10.1029/WR017i002p00295

Kanda M, Inagaki A, Letzel MO, Raasch S, Watanabe T (2004) LES study of the energy imbalance problem with eddy covariance fluxes. Boundary-Layer Meteorol 110:381–404

Kang SL, Davis KJ (2008) Effects of mesoscale surface heterogeneity on the fair-weather convective atmospheric boundary layer. J Atmos Sci 65:3197–3213

Katul GG, Sempreviva AM, Cava D (2008) The temperature–humidity covariance in the marine surface layer: a one-dimensional analytical model. Boundary-Layer Meteorol 126:263–278

Lai CT, Ehleringer JR, Bond BJ, KT Paw U (2005) Contributions of evaporation, isotopic non-steady state transpiration, and atmospheric mixing on the $\delta^{18}O$ of water vapor in Pacific Northwest coniferous forests. Plant Cell Environ 29:77–94

Lai C, Schauer A, Owensby C, Ham J, Helliker B, Tans P, Ehleringer J (2006) Regional CO_2 fluxes inferred from mixing ratio measurements: estimates from flask air samples in central Kansas, USA. Tellus 58B:523–536

Lee X, Massman W (2011) A perspective on thirty years of the Webb, Pearman and Leuning density corrections. Boundary-Layer Meteorol 139:37–59

Lee X, Smith R, Williams J (2006) Water vapor $^{18}O/^{16}O$ isotope ratio in surface air in New England, USA. Tellus 58B:293–304

Lee X, Kim K, Smith RB (2007) Temporal variations of the $^{18}O/^{16}O$ signal of the whole-canopy transpiration in a temperate forest. Glob Biogeochem Cycles 21:GB3013. doi:10.1029/2006GB002871

Lee X, Griffis TJ, Baker JM, Billmark KA, Kim K, Welp LR (2009) Canopy-scale kinetic fractionation of atmospheric carbon dioxide and water vapor isotopes. Glob Biogeochem Cycles 23:GB1002. doi:10.1029/2008GB003331

Lloyd J, Francey R, Mollicone D, Raupach M, Sogachev A, Arneth A, Byers J, Kelliher F, Rebmann C, Valentini R, Wong S, Bauer G, Schulze E (2001) Vertical profiles, boundary layer budgets, and regional flux estimates for CO_2 and its $^{13}C/^{12}C$ ratio and for water vapor above a forest/bog mosaic in central Siberia. Glob Biogeochem Cycles 15:267–284

Moeng C (1984) A large-eddy-simulation model for the study of planetary boundary-layer turbulence. J Atmos Sci 41:2052–2062

Moeng CH, Wyngaard JC (1984) Statistics of conservative scalars in the convective boundary layer. J Atmos Sci 41:3161–3169

Ogée J, Peylin P, Ciais P, Bariac T, Brunet Y, Berbigier P, Roche C, Richard P, Bardoux G, Bonnefond JM (2003) Partitioning net ecosystem carbon exchange into net assimilation and respiration using $^{13}CO_2$ measurements: a cost-effective sampling strategy. Glob Biogeochem Cycles 17:1070. doi:10.1029/2002GB001995

Ogée J, Peylin P, Cuntz M, Bariac T, Brunet Y, Berbigier P, Richard P, Ciais P (2004) Partitioning net ecosystem carbon exchange into net assimilation and respiration with canopy-scale isotopic measurements: an error propagation analysis with $^{13}CO_2$ and $C^{18}OO$ data. Glob Biogeochem Cycles 18:GB2019

Pataki DE, Bowling DR, Ehleringer JR, Zobitz JM (2006) High resolution atmospheric monitoring of urban carbon dioxide sources. Geophys Res Lett 33:L03813

Patton EG, Sullivan PP, Davis KJ (2003) The influence of a forest canopy on top-down and bottom-up diffusion in the planetary boundary layer. Q J Roy Meteorol Soc 129:1415–1434

Patton EG, Sullivan PP, Moeng CH (2005) The influence of idealized heteorogeneity on wet and dry planetary boundary layers coupled to the land surface. J Atmos Sci 62:2078–2097

Riley WJ, Still CJ, Torn MS, Berry JA (2002) A mechanistic model of $H_2{}^{18}O$ and $C^{18}OO$ fluxes between ecosystems and the atmosphere: Model description and sensitivity analyses. Glob Biogeochem Cycles 16:1095–1109. doi:10.1029/2002GB001878
Ronda R, De Bruin H, Holtslag A (2001) Representation of the canopy conductance in modeling the surface energy budget for low vegetation. J Appl Meteorol 40:1431–1444
Roth M, Oke TR (1995) Relative efficiencies of turbulent transfer of heat, mass and momentum over a patchy urban surface. J Atmos Sci 52:1863–1874
Scanlon TM, Kustas WP (2010) Partitioning carbon dioxide and water vapor fluxes using correlation analysis. Agric For Meteorol 150:89–99
Steinfeld G, Letzel MO, Raasch S, Kanda M, Inagaki A (2007) Spatial representativeness of single tower measurements and the imbalance problem with eddy-covariance fluxes: results of a large-eddy simulation study. Boundary-Layer Meteorol 123:77–98
Still CJ et al (2009) Influence of clouds and diffuse radiation on ecosystem-atmosphere CO_2 and $C^{18}OO$ exchanges. J Geophys Res 114:G01018. doi:10.1029/2007JG000675
Sullivan P, Moeng C, Stevens B, Lenschow D, Mayor S (1998) Structure of the entrainment zone capping the convective atmospheric boundary layer. J Atmos Sci 55:3042–3064
Tans PP (1980) On calculating the transfer of ^{13}C in reservoir models of the carbon cycle. Tellus 32:464–469
Welp LR, Lee X, Kim K, Griffis TJ, Billmark K, Baker JM (2008) $\delta^{18}O$ of water vapor, evapotranspiration and the sites of leaf water evaporation in a soybean canopy. Plant Cell Environ 31:1214–1228
Wen XF, Zhang SC, Sun XM, Yu GR, Lee X (2010) Water vapor and precipitation isotope ratios in Beijing, China. J Geophys Res Atmos 115:D01103. doi:10.1029/2009JD012408
Williams DG, Cable W, Hultine K et al (2004) Evapotranspiration components determined by stable isotope, sap flow and eddy covariance techniques. Agric For Meteorol 125:241–258
Wilson KB, Hanson PJ, Mulholland PJ, Baldocchi DD, Wullschleger SD (2001) A comparison of methods for determining forest evapotranspiration and its components: sap-flow, soil water budget, eddy covariance and catchment water balance. Agric For Meteorol 106:153–168
Xiao W, Lee X, Griffis T, Kim K, Welp L, Yu Q (2010) A modeling investigation of canopy–air oxygen isotopic exchange of water vapor and carbon dioxide in a soybean field. J Geophys Res Biogeosci 115:G01004. doi:10.1029/2009JG001,163
Yakir D, Sternberg LSL (2000) The use of stable isotopes to study ecosystem gas exchange. Oecologia 123:297–311
Zobitz JM, Burns SP, Reichstein M, Bowling DR (2008) Partitioning net ecosystem carbon exchange and the carbon isotopic disequilibrium in a subalpine forest. Glob Chang Biol 14:1785–1800